

Submillimeter-Accurate 3D Lumbar Spine Reconstruction from Biplanar X-Ray Images: Incorporating a Multi-Task Network and Landmark-Weighted Loss

Wanxin Yu [1,2], Zhemin Zhu [4], Cong Wang [4], Yihang Bao [1,2], Chunjie Xia[1,2], Rongshan Cheng [1,2]*, Yan Yu [3]*, Tsung-Yuan Tsai [1,2,4]*

¹ *School of Biomedical Engineering & Med-X Research Institute, Shanghai Jiao Tong University, Shanghai 200030, China*

² *Engineering Research Center of Digital Medicine and Clinical Translation, Ministry of Education, Shanghai 200030, China*

³ *Department of Spine Surgery, Tongji Hospital, School of Medicine, Tongji University, Shanghai, 200065, China.*

⁴ *TAOiMAGE Medical Technologies Corporation, Shanghai 200120, China*

***Corresponding Author:**

Rongshan Cheng, *School of Biomedical Engineering & Med-X Research Institute, Shanghai Jiao Tong University, Shanghai 200030, China. Email: chengrongshan@sjtu.edu.cn*

Yan Yu, *Department of Spine Surgery, Tongji Hospital, School of Medicine, Tongji University, Shanghai, 200065, China. E-mail: yyu15@tongji.edu.cn*

Tsung-Yuan Tsai, *School of Biomedical Engineering & Med-X Research Institute, Shanghai Jiao Tong University, Shanghai, 200030, China. Email: tytsai@sjtu.edu.cn*

Highlights:

- Achieved sub-millimeter (0.80 ± 0.15 mm) accuracy in lumbar 3D reconstruction, which is significantly superior to existing methods.
- A multi-task network for lumbar decomposition and landmark detection, improving prediction accuracy.
- A landmark-weighted reconstruction loss function, enhancing 3D reconstruction accuracy.
- 3D reconstruction accuracy was validated using registration-derived gold standards.

List of abbreviations: 3D, three-dimensional; 2D, two-dimensional; SSM, statistical shape model; DRR, Digitally Reconstructed Radiograph; CT, Computed Tomography; MRI, Magnetic Resonance Imaging; 6-DOF, six degree of freedom; AP, anteroposterior; LAT, lateral; PCA, principal component analysis; GPA, generalized Procrustes analysis; FFM, feature fusion module; NCC, normalized cross-correlation; MAE, simple mean absolute error; PSNR, Peak Signal-to-Noise Ratio; SSIM, structural similarity index measure; SDR, success detection rate; MAE, mean absolute error; GAN, generative adversarial network;

Abstract:

Three-dimensional reconstruction of the spine under weight-bearing conditions from biplanar X-ray images is of great importance for the clinical assessment of spinal diseases. However, the current fully automated reconstruction methods only achieve millimeter-level accuracy, making it difficult to meet clinical standards. This study developed and validated a fully automated method for high-accuracy 3D reconstruction of the lumbar spine from biplanar X-ray images. The method involves lumbar decomposition and landmark detection from the raw X-ray images, followed by a deformable model and landmark-weighted 2D-3D registration approach. The reconstruction accuracy was validated by the gold standard obtained through the registration of CT-segmented vertebral models with the biplanar X-ray images. The proposed method achieved a 3D reconstruction accuracy of 0.80 ± 0.15 mm, representing a significant improvement over the mainstream approaches. This study will contribute to the clinical diagnosis of lumbar in weight-bearing positions.

Keywords: 3D Reconstruction; Lumbar spine; biplanar X-rays

1 Introduction

The lumbar spine is the most heavily loaded part of the spine, and its pathological conditions are often accompanied by changes in three-dimensional (3D) morphology and structure, such as lumbar disc herniation and spondylolisthesis. Therefore, understanding the 3D alignment of the lumbar spine and the morphology of the vertebral bodies is crucial for the clinical diagnosis of spinal diseases. For instance, the height and endplate area of the vertebral bodies can help detect vertebral fractures, collapse, or deformities (Wang et al., 2020; Wáng et al., 2018). Abnormal intervertebral disc space may indicate issues such as intervertebral disc degeneration, herniation, or protrusion (Galbusera et al., 2014). Moreover, understanding the 3D curvature of the spine can be beneficial for diagnosing scoliosis and for surgical planning (Liang et al., 2024). The 3D structure of the lumbar spine in the standing position can better reveal the anterior displacement of the vertebral bodies, aiding in the detection of degenerative lumbar spondylolisthesis (Matz, 2016). The patient-specific 3D anatomy of the lumbar spine can help measure vertebral geometry and pathological deformities, assisting in disease assessment, surgical planning, and implant design (Sarkalkan et al., 2014). The 3D parameters of the weight-bearing lumbar spine hold greater clinical value for diagnosis and surgical planning (Hasegawa et al., 2018). However, there is currently a lack of automated imaging devices or methods to establish the 3D structure of the patient's weight-bearing spine. Traditional X-rays only provide two-dimensional (2D) information and are prone to issues such as anatomical structure overlap and projection distortion. The anatomical parameters measured from X-rays are insufficient to accurately reflect the true condition (Gupta et al., 2016, 2015). Conventional 3D medical imaging techniques, such as CT and MRI, primarily depict 3D morphology in the supine position (Wybier and Bossard, 2013), and have drawbacks including high radiation exposure, high costs, lengthy imaging times, and the necessity for manual segmentation and reconstruction (Yu et al., 2016). These traditional medical imaging methods require physicians to perform clinical parameter measurements, which can be time-consuming, laborious, and exhibit poor reproducibility. Consequently, fully automated 3D reconstruction of the lumbar spine based on biplanar orthogonal X-ray images has emerged as a low-cost and safe solution for obtaining 3D parameters of the lumbar spine in the standing position. This method can be applied to evaluate disc herniation and lumbar spondylolisthesis under load, as well as for repetitive follow-up imaging and pediatric assessments (Ghenot et al., 2012).

Currently, there are two main approaches for reconstructing the 3D bone structure from biplanar X-ray images: end-to-end reconstruction based on machine learning and registration-based reconstruction using deformable models. The former approach suffers from low reconstruction accuracy ($>3\text{mm}$) due to the lack of prior shape information about the reconstructed structure and the limited information provided by the biplanar images (Chen et al., 2023). The latter approach begins with encoding the prior appearance information of the anatomical structure (Markelj et al., 2012). It then uses a set of parameters to manipulate the model and adjust the deformable model parameters based on the patient's X-ray images, achieving high-precision patient-specific 3D reconstruction (Fang et al., 2020; Yu et al., 2016). There are two main strategies for finding the optimal parameters in this approach. The first involves identifying landmarks in the X-ray images, establishing correspondence between the deformable model and the landmarks, and minimizing the geometric distance between them (Aubert et al., 2019; Karade and Ravi, 2015). The methods for identifying landmarks range from fully manual to fully automatic; however, the manual annotation method is very time-consuming. Conversely, fully automatic methods tend to have larger errors and are more prone to mistakes (Reyneke et al., 2019; Yu et al., 2016). The second method is based on

digitally reconstructed radiograph (DRR), which projects the deformable model as a whole onto the 2D plane of the X-ray image to obtain a simulated X-ray image. This method iteratively improves the similarity between the raw X-ray image and the DRR to obtain best-fitting parameters for the deformable model (Aubert et al., 2023; Klima et al., 2016; Väänänen et al., 2015; Yu et al., 2016). The DRR-based method is more accurate than the feature-based method, but it takes several minutes to compute and is more prone to getting stuck in local optima (Markelj et al., 2012; Miao et al., 2016).

As a technology used to assist clinical diagnosis, the primary goal of 3D reconstruction of human anatomical structures based on simultaneous acquisition of anteroposterior (AP) and lateral (LAT) radiographic images is to achieve higher accuracy. Taking the lumbar spine as an example, the existing publicly available methods based on variable models can achieve an accuracy of around 1.0–2.0 mm (Table 1). However, such effects are still insufficient to meet clinical needs. Measurement errors for vertebral height and disc thickness should be within 1 mm, and diagnostic precision for spinal canal stenosis must reach submillimeter levels to avoid missed or incorrect diagnoses (de Schepper et al., 2013; Tan et al., 2013). Besides, current methods often overlook detailed anatomical structures, such as the transverse and spinous processes of the lumbar spine. This can result in models that emphasize the larger vertebral bodies during the 2D-3D registration process while neglecting the more complex structures of the vertebral arches. Most importantly, the ground truth used to evaluate the 3D reconstruction results in current research cannot be regarded as the gold standard. Some studies utilize CT/MRI segmentation results as the validation standard, which cannot verify the 3D positioning of the spine (Bennani et al., 2022; Fang et al., 2020). Other studies employ semi-automatic reconstructions with manually adjusted shapes as the validation standard, which fail to confirm the 3D shape information of the vertebra (Aubert et al., 2023, 2019).

Table 1. Performance Metrics of Variable Model-Based Lumbar Spine 3D Reconstruction Methods.

| Study | Reconstruction Accuracy (mm) | Time Taken | Automation Level | Validation Standard |
|--------------------------|------------------------------|------------|------------------|-----------------------------------|
| (Fang et al., 2020) | 1.2 | 3 minutes | Semi-automatic | CT reconstructed model |
| (Bennani et al., 2022) | 1.7–2.0 | - | Semi-automatic | CT reconstructed model |
| (Whitmarsh et al., 2013) | 0.93–1.34 | 4.3 hours | Semi-automatic | CT reconstructed model |
| (Aubert et al., 2019) | 1.9–2.2 | 34 seconds | Fully automatic | Manual deformation reconstruction |

| | | | | |
|--------------------------|---------|----------|--------------------|--------------------------------------|
| (Aubert et al., 2023) | 1.3-1.6 | <1minute | Fully automatic | Manual deformation reconstruction |
|--------------------------|---------|----------|--------------------|--------------------------------------|

In summary, current 3D lumbar spine reconstruction from biplanar X-rays faces challenges related to insufficient accuracy to meet clinical requirements and a lack of focus on complex vertebral arch structures. Additionally, there is no gold standard for evaluating the results. This study aims to improve the 3D reconstruction accuracy of the lumbar spine to sub-millimeter levels by pre-processing X-rays with lumbar decomposition and landmark detection, and employing a landmark-weighted approach to complete the 2D-3D registration of the deformable model. The outcomes will be validated against CT segmentation and biplanar X-ray registration results as the gold standard.

2 Materials and Methods:

2.1. Data

The study was approved by the institutional review board (protocol number: 2021-011-SK). In this study, 175 lumbar CT scan datasets (United Imaging, uCT760, 120 kV, 512×512 resolution, 1.0 mm slice spacing) were collected from Shanghai Tongji Hospital (Table 2). All participants had no prior diagnosis of spinal disease. Subjects with abnormal osteophyte formation, obvious vertebral deformity, or fracture were excluded from the study. Written informed consent was obtained from all participants before collecting any personal or health-related data. The CT images were imported into the 3D visualization and modeling software Amira 6.7 (Thermo Fisher Scientific, Rockford, IL, United States), where an experienced orthopedic surgeon segmented the L1-L5 vertebrae and annotated seven bony landmarks (superior endplate center, inferior endplate center, left transverse process, right transverse process, left pedicle, right pedicle, spinous process) on each lumbar vertebra.

In addition to the CT scans, biplanar X-ray images (GOLDEN EYE, TAOiMAGE, Shanghai, China; image resolution 3072×3072 pixels) of the lumbar spine were acquired for 50 of the participants (Table 2). The participants were asked to perform six degrees of freedom (6-DOF) lumbar movements (flexion, extension, left/right bending, left/right rotation) at three different levels, and the corresponding biplanar X-ray images were captured simultaneously. Participants practiced the tasks beforehand to familiarize themselves. During the experiment, all participants wore lead protective clothing in non-imaging areas to reduce unnecessary radiation exposure. Approximately 18 pairs of fluoroscopic projections were taken for each participant. According to the manufacturer's product manual, the effective dose for each pair of lumbar images under our typical test conditions (78 kV, 40 mA) was 0.16 mSv, which is less than 2.88 mSv per test, or about 14.4% of the average annual occupational exposure limit.

Table 2. Subject demographics data.

| Variables | CT (N=175) | CT+ X-ray (N=50) |
|-------------|------------|------------------|
| Gender(M:F) | 82:93 | 18:32 |

| | | |
|-------------------------|-----------|-----------|
| Age(year) | 37.6±10.7 | 23.7±2.1 |
| Height(m) | 1.67±0.06 | 1.68±0.06 |
| Weight(kg) | 64.3±11.6 | 61.4±10.7 |
| BMI(kg/m ²) | 23.6±3.7 | 21.8±2.5 |

To generate training labels for deep learning and evaluate the 3D reconstruction, the biplanar X-ray images were registered with the 3D CT-segmented L1-L5 vertebral models of the same participants. A custom registration program (MATLAB, R2023a, MathWorks, Natick, MA, United States) was used to adjust the 3D position and rotation of each vertebra until it matched the corresponding contours in the biplanar images. This technique has been validated as a gold standard, with a repeatability of less than 0.3 mm in translation and less than 0.7° in orientation

when reproducing in-vivo human spine 6DOF kinematics (Li et al., 2009). Simulated projections were then conducted in the registered environment to generate DRRs of the same size as the raw images (Pointon et al., 2023). The simulation adhered to the Beer-Lambert law, treating the vertebrae as homogeneous structures with a Hounsfield unit of 800, which represents the average density of the lumbar spine. Additionally, the expert-annotated 3D vertebral landmark coordinates were projected onto the 2D images, and their 2D coordinates were calculated. This provided the labeled data necessary for deep learning training.

2.2. Statistical modeling

Due to the lack of original information, it is necessary to introduce prior shape information about the object to be reconstructed to achieve an ideal reconstruction effect. This study used a statistical shape model (SSM) as the prior information for the 3D shape of the vertebrae. Since vertebrae exhibit shape differences at different levels, we have established separate SSMs for the L1-L5 vertebrae (Fig. 1). First, a reference mesh was selected. Then, rigid transformations were applied to each target mesh to align it as closely as possible with the reference mesh. Next, non-rigid alignment was performed on the reference mesh to fit it to each target mesh (Audenaert et al., 2019). Finally, principal component analysis (PCA) was conducted on all the aligned meshes, and landmarks were annotated on the resulting average model.

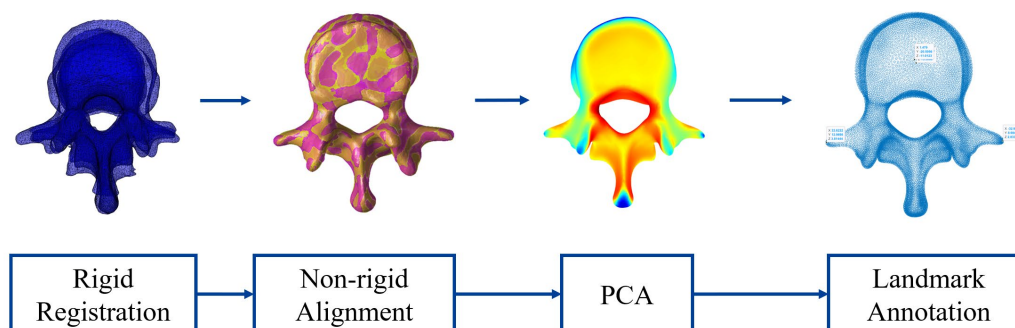


Fig. 1. Workflow for Establishing a SSM of Vertebrae

In the specific implementation process, individual vertebrae were adaptively re-meshed to increase vertex density in regions with greater geometric variation. Since the time consumed by the

adopted DRR method is not affected by the number of model vertices, we selected the mesh with a vertex count closest to 10,000 as the reference to ensure the final statistical model preserves vertebral shape details.

Initial rigid alignment was achieved by establishing local vertebral coordinate systems using bony landmarks and transforming vertex coordinates accordingly. Rigid alignment was further refined with an optimized ICP algorithm to exclude outlier correspondences, followed by generalized Procrustes analysis (GPA) without scaling, preserving vertebral size as an important mode in the subsequent principal component analysis. Non-rigid alignment was performed by approximating the vertex displacement between the reference and target meshes using Gaussian radial basis functions with thin plate spline interpolation (Audenaert et al., 2019).

At last, we performed PCA on all the aligned meshes:

$$S = \bar{S} + Pb \quad (1)$$

The shape vector S represents the ordered arrangement of the vertex coordinates of the vertebral surface mesh. \bar{S} represents the corresponding mean shape, P is the covariance matrix, and b are the eigenvectors. By adding different deformation modes to the mean shape, we can generate different shapes of the vertebral surface model.

Similar to the annotated landmarks on the vertebral model, we asked the same orthopedic surgeon to annotate four anatomical landmarks—the centers of the superior and inferior endplates and the tips of the left and right transverse processes—for L1–L5 on the SSM, to facilitate subsequent registration tasks.

2.3 X-ray image preprocessing

Traditional 3D reconstruction methods rely on raw X-ray images for registration, which can encounter issues such as getting stuck in local minima and exhibiting low registration accuracy (Reyneke et al., 2019). With advancements in computer vision, recent research has proposed performing style transfer on raw X-ray images to achieve high-precision registration (Aubert et al., 2023). This study involved multi-task processing for lumbar decomposition and vertebral landmark detection using raw biplanar X-ray images. This approach extracts the necessary information for subsequent registration while minimizing interference from other pixels in the image. The encoder portion of the convolutional neural network employed shared parameters to conserve computational resources. The decoder was divided into two paths: one for lumbar decomposition and the other for vertebral landmark detection. Additionally, a feature fusion module (FFM) was implemented to combine the features from both tasks. Finally, their respective output heads were utilized to finalize the results of the two tasks (Fig. 2).

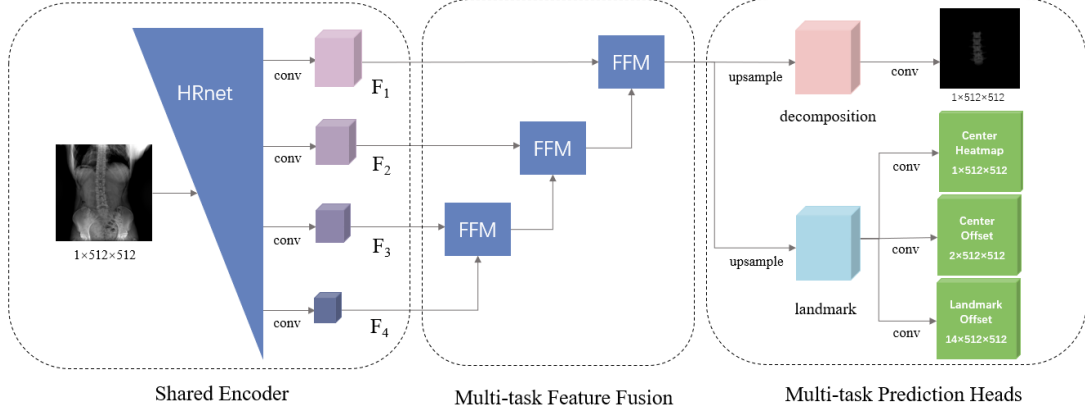


Fig. 2. Architecture of the multi-task processing network for lumbar decomposition and vertebral landmark detection

Encoder: Compared with widely used backbone networks such as ResNet, UNet, and DeepLab, which tend to lose detailed spatial information due to repeated downsampling, HRNet maintains high-resolution representations throughout the feature extraction process (Sun et al., 2019). This capability allows the model to better capture spatial details and edge information, which is critical for accurate prediction in tasks with fine-grained requirements. We adopt HRNet-W48 as the encoder of the multi-task prediction network. HRNet-W48 has four stages with parallel multi-resolution branches, outputting feature maps at $1/4$, $1/8$, $1/16$, and $1/32$ of the input size ($\{F_1, F_2, F_3, F_4\}$), with channel numbers [48, 96, 192, 384]. This architecture better preserves spatial details and improves prediction accuracy compared to conventional backbones.

Decoder: The decoder employs a U-Net-like architecture, separating features through convolutional layers to obtain the decomposition path and the landmark path. The features in the two paths are then upsampled and progressively decoded. We posit that there are significant interdependencies between lumbar decomposition results and vertebral landmark locations. To leverage this relationship, we designed the FFM to explicitly incorporate spatial dependencies between the two decoding pathways, thereby enhancing the predictive accuracy of both tasks (Fig. 3). The FFM is executed three times during the decoding process. The decomposition features and landmark features are input to the FFM, which first uses element-wise summation to fuse the information between the decomposition and landmark paths. Next, convolution operations extract the spatial dependencies from the fused feature map, effectively employing trainable parameters for image alignment. The fused feature map is then concatenated with the original feature maps of the decomposition and landmark paths to ensure that no information is lost. Convolution operations are subsequently performed to maintain consistency in the number of channels with the input feature maps. Finally, upsampling is carried out, and element-wise summation with the previous level feature map is performed to introduce higher-dimensional features, which are then input into the next stage of decoding.

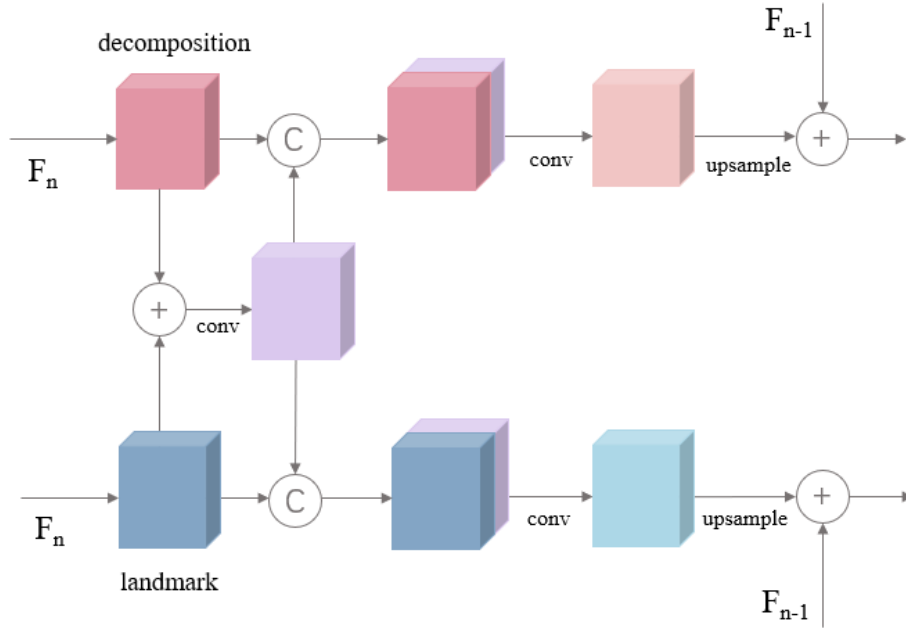


Fig. 3. A block diagram of the two-task feature fusion module

Mapping layer: The network output was divided into the results of lumbar decomposition and the detection of seven landmarks on each lumbar vertebra. The lumbar decomposition result is a 512×512 grayscale image, while the landmark detection result includes the heatmap of the vertebral centers, the center offset vector map, and the landmark offset vector map. Due to the complex X-ray structure of the lumbar region, directly obtaining the coordinates of the landmarks is challenging. Therefore, we transformed the landmark detection task into predicting the position of the center point of each vertebra and the offset vector of each landmark. This approach has the advantage of ensuring that the predicted results for the vertebral centers do not overlap. Additionally, there is a dependence between the vertebral centers and the positions of the landmarks, which enhances the accuracy of landmark detection (Yi et al., 2020).

Loss: The total regression loss is comprised of two parts: lumbar decomposition and landmark detection. For the lumbar decomposition component, we employed the normalized cross-correlation (NCC) loss and the L_2 loss as the optimization functions. The NCC loss effectively detects local features or patterns in the image, and it is defined as:

$$L_{NCC} = \frac{\sum_{i=1}^N (I_{gt}^i - \overline{I_{gt}}) (I_p^i - \overline{I_p})}{\sqrt{\sum_{i=1}^N (I_{gt}^i - \overline{I_{gt}})^2 \cdot \sum_{i=1}^N (I_p^i - \overline{I_p})^2}} \quad (2)$$

Here, N represents the total number of pixels in the image, I_{gt}^i and I_p^i represent the pixel values of the ground truth image and the predicted image respectively, and $\overline{I_{gt}}$ and $\overline{I_p}$ represent their respective means. Since we want the output to be the projection image of the lumbar vertebrae, we need not only to segment the position of the lumbar vertebrae but also to convert it to the DRR projection style. Therefore, we also employ a simple L_2 loss:

$$L_{L2} = \frac{1}{N} \sum_{i=1}^N (I_{gt}^i - I_p^i)^2 \quad (3)$$

The landmark detection loss includes the vertebral center heatmap loss L_{hm} , the center offset loss L_{co} , and the landmark offset loss L_{lo} . L_{hm} is defined as:

$$L_{hm} = - \sum_{i=1}^N [I(I_{gt}^i = 1) \cdot \log(I_p^i) \cdot (1 - I_p^i)^2 + I(I_{gt}^i < 1) \cdot (1 - I_p^i)^4 \cdot \log(1 - I_p^i) \cdot I_p^i] \quad (4)$$

Where $I(\cdot)$ is the indicator function. L_{hm} can give greater weight to samples that are difficult to classify when dealing with imbalanced datasets, thereby improving the robustness of the model. L_{co} and L_{lo} both use a simple L1 loss:

$$L_{co} = \frac{1}{5} \sum_{i=1}^5 |c_{gt}^i - c_p^i| \quad (5)$$

$$L_{lo} = \frac{1}{35} \sum_{i=1}^{35} |l_{gt}^i - l_p^i| \quad (6)$$

Where c_{gt}^i and c_p^i are the ground truth and predicted values of the offset coordinates of the centers of the five lumbar vertebrae, respectively, and l_{gt}^i and l_p^i are the ground truth and predicted values of the offset coordinates of the 35 feature points on the five lumbar vertebrae, relative to their corresponding vertebral centers. We introduced the weight hyperparameters $\lambda_{NCC}, \lambda_{L2}, \lambda_{hm}, \lambda_{co}, \lambda_{lo}$ to balance the scale and importance of each loss term, resulting in the following total training loss function:

$$\text{Loss} = \lambda_{NCC} L_{NCC} + \lambda_{L2} L_{L2} + \lambda_{hm} L_{hm} + \lambda_{co} L_{co} + \lambda_{lo} L_{lo} \quad (7)$$

2.4 Automatic 3D Reconstruction

We complete the fully automatic 3D reconstruction of the lumbar vertebrae through 2D-3D registration of the SSM and the lumbar decomposition image. The five vertebrae are optimized simultaneously to address the issue of overlap in the images. To improve registration efficiency and prevent the process from getting stuck in a local optimum, we first initialize the pose of each vertebra. Using the projection environment of the biplanar system and the positions of the vertebral landmarks predicted by the network, we can calculate the optimal fitting positions of these landmarks in 3D space using the least squares method:

$$I = O_1 + \hat{x}_0 \cdot (P_1 - O_1) \quad (8)$$

$$\hat{x} = \underset{x}{\operatorname{argmin}} ||Ax - b||^2$$

Where $A = \begin{bmatrix} P_1 - O_1 \\ O_2 - P_2 \end{bmatrix}$, $b = O_2 - O_1$. O_1, O_2 are the 3D coordinates of the radiation sources for the AP and LAT views, respectively. P_1 and P_2 are the 3D coordinates of the same landmark on the AP and LAT detectors, respectively. By calculating the transformation matrix for each lumbar vertebra based on the reconstructed 3D landmarks, we can transform the vertex coordinates of the 5 lumbar vertebrae SSMs to their estimated initial positions within the biplanar projection environment.

The next step is to perform the 2D-3D registration process. For each vertebra, it is necessary to optimize its 6-DOF rigid transformation parameters and the non-rigid transformation parameters controlled by the principal components. Based on Cattell's Scree Test analysis, we selected the first 14 principal components, which cover 75% of the variance patterns (Fig. 4).

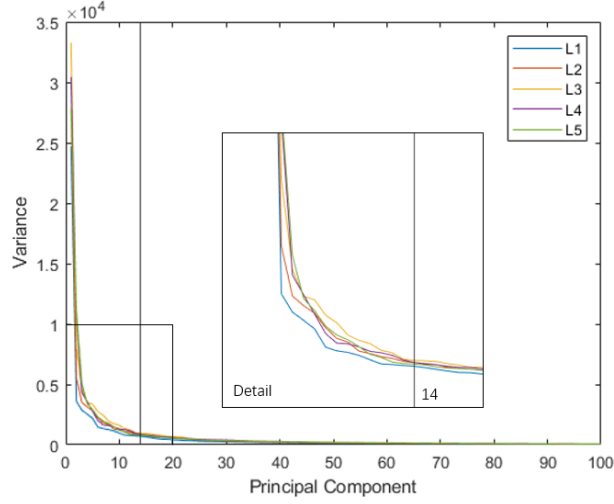


Fig. 4. Scree plot of the SSM for the L1-L5 vertebrae. The inflection point is at the 14th principal component.

We constrained the range of the parameter search based on the accuracy of pre-alignment. Translation along the three orthogonal axes was limited to $\pm 10\text{mm}$, axial rotation around the y-axis was limited to $\pm 30^\circ$, and rotations in the other two directions were limited to $\pm 15^\circ$. The deformation of each principal component was confined within three standard deviations. During the registration process, a new shape model instance was constructed by searching for the rigid transformation and non-rigid deformation parameters of the shape model. DRRs of the generated instances were then created, with the projection parameters consistent with those used for generating vertebrae separation labels. Each time a new single lumbar vertebra instance is generated, it can be represented as:

$$S = \left(\bar{S} + \sum_{i=1}^{14} P_i b_i \right) \cdot T \quad (9)$$

where \bar{S} denotes the mean shape model of the lumbar vertebra, P_i is the covariance matrix of its i -th principal component, b_i is the eigenvector of its i -th principal component, and T is the 3D transformation matrix established according to its 6-DOF rigid transformation parameters.

The optimization goal during the 3D reconstruction process is to maximize the similarity between the biplanar DRR images and the lumbar decomposition images. Since the raw X-ray images have already been converted into DRR style, we chose a simple mean absolute error (MAE) loss as the image similarity metric. To emphasize the significance of the spinous and transverse processes during reconstruction, we customized a weighting matrix based on the landmark positions. The total weighted loss function can be expressed as:

$$Loss = \sum_{i=\{AP, LAT\}} |I_{pred}^i - I_{DRR}^i| \cdot W^i \quad (10)$$

Where I_{pred} is the predicted lumbar decomposition image, I_{DRR} is the DRR generated by the current model, and W is the weight matrix of the same size as the image. We applied weighting to the positions of the transverse processes and spinous processes on W using a gaussian point spread function:

$$W(x, y) = \sum_{i=1}^{15} \frac{1}{2\pi\sigma^2} e^{-\frac{(x-x_i)^2+(y-y_i)^2}{2\sigma^2}} + \lambda \quad (11)$$

Where (x_i, y_i) are the landmark coordinates output by the network. (x, y) are the points on the weight matrix. The generation radius for the weighting region is defined as d , which corresponds to the distance between the transverse process or spinous process and the pedicle landmark. Thus, $x \in [x_i - d, x_i + d], y \in [y_i - d, y_i + d]$. λ denotes the base weight and σ the standard deviation; through parameter tuning, they are set to 0.3 and 10, respectively. We focus on a pair of transverse processes and spinous processes for each vertebra, resulting in a total of $3 \times 5 = 15$ landmarks were used to assign weights.

Our objective function is non-convex and has multiple local extrema, which requires the optimizer to demonstrate high robustness against noise and irregular objective functions, as well as global convergence capability. Therefore, we selected the BOBYQA (Bound Optimization BY Quadratic Approximation) derivative-free optimization algorithm from the NLOpt nonlinear optimization library for the registration process.

3 Experiments and results

3.1 SSMs of lumbar vertebrae

We constructed a SSM for L1-L5 vertebrae using CT segmentation data from 175 individuals, analyzing its specificity and generality. The proposed method was implemented through a custom program (MATLAB, R2023a MathWorks, Natick, MA, United States). Specificity measures the model's ability to generate shapes similar to instances in the training set and is defined as the matching distance between uniformly randomly generated shapes and their closest matches in the training set (Fig. 5 (left)). Generality measures the model's ability to generate new instances, validated using the leave-one-out method, which is defined as the average error of all leave-one reconstructions (Fig. 5 (right)) (Reyneke et al., 2019). As the number of principal components increases, specificity gradually improves while generality decreases, indicating that more principal components enable the model to better adapt to different scenarios.

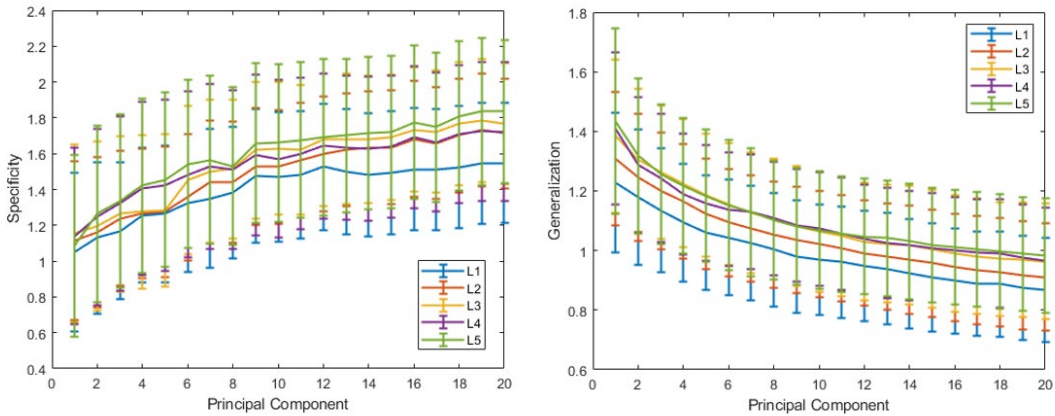


Fig. 5. The functional relationship between the specificity (left) and generality (right) of the L1-L5 vertebral SSM and the number of principal components.

Fig. 6 illustrates the deformation of the statistical shape model of the L1 vertebra under three

times the standard deviation of the first three principal components. The first principal component primarily represents the size of the vertebra, the second principal component mainly characterizes the width of the transverse processes, and the third principal component primarily reflects the thickness of the lamina, among other features.

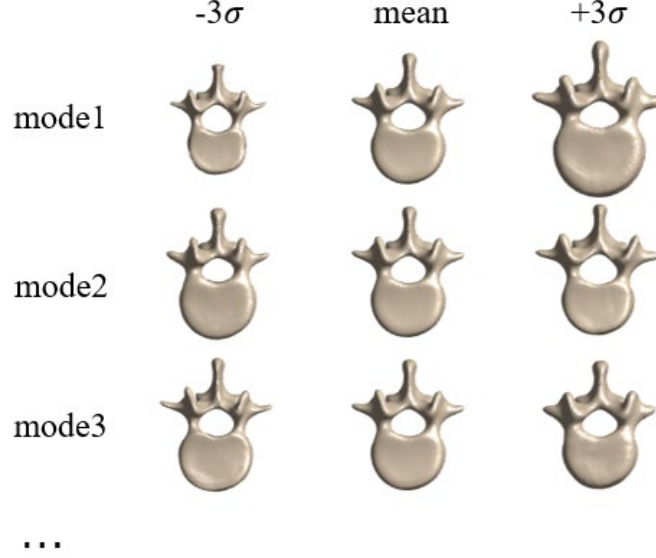


Fig. 6. The average of the SSM of the L1 vertebra from a top view and the first three variation modes, described using the average \pm three times the standard deviation.

3.2 X-ray image preprocessing

Dataset: We collected biplanar X-ray images of the lumbar region from 50 individuals with 6-DOF, resulting in 900 pairs of biplanar images along with corresponding lumbar decomposition images and landmark annotations obtained after registration. Among the participants, two individuals had specific conditions: L2-L3 vertebral fusion and lumbar sacralization, which we designated as special test data. From the remaining 48 individuals, we randomly selected 8 individuals' 144 pairs of dual-plane images to form the test set, while the remaining 40 individuals' 720 pairs of data were used for the training and validation set. We employed five-fold cross-validation to tune the hyperparameters. Prior to training, all data were converted to a resolution of 512×512 pixels, with a corresponding pixel spacing of 0.834×0.834 mm.

Experimental settings: The proposed method was implemented using the PyTorch framework, and the training process was conducted on a workstation equipped with four NVIDIA GeForce RTX 3070 GPUs (with 24GB main memory). The optimizer used was AdamW, which separates weight decay from gradient updates, providing better regularization effects. The initial learning rate was set at 0.001, with a total of 300 training epochs, and the learning rate decayed to 0.9 times the original rate every 20 epochs. Additionally, we performed random flipping and rotation on the training set to increase data diversity, enhance the model's generalization capability, and improve robustness.

Evaluation metrics: For the lumbar decomposition task, we employed three performance metrics to quantitatively evaluate the proposed method: Dice coefficient (Dice), peak signal-to-noise ratio (PSNR), and structural similarity index measure (SSIM). Dice is commonly used to assess image segmentation tasks, while PSNR and SSIM measure the results of image style transfer

in DRR. In the landmark detection task, we utilized mean distance and success detection rate (SDR) to evaluate the model's predictions. Mean distance refers to the Euclidean distance between predicted landmark coordinates and ground truth. SDR indicates the success prediction rates for mean distances within 2mm, 4mm, and 6mm, respectively.

Experimental results: The results of the proposed method for lumbar decomposition are shown in Table 3, while the landmark detection results are presented in Tables 4 and 5. We compared our method to HRNet for single decomposition task and single landmark detection task, finding that our method achieved superior outcomes in the lumbar decomposition task, with a Dice coefficient of 99.5%, a PSNR of 45.8, and a SSIM of 99.2%. The proposed method also demonstrated high accuracy in the landmark detection task, achieving an overall detection accuracy of 2.34 mm for AP images and 4.03 mm for LAT images. Unlike traditional landmark detection, which focuses on clearly defined features like vertebral corners, detecting transverse and spinous processes presents challenges such as occlusion and low gradients in the AP and LAT images, making detection more difficult. The results indicate that detecting features in LAT images is more challenging than in AP images, and the performance for the endplate center and pedicle is better than that for the transverse and spinous processes.

Notably, our proposed method utilized the same network to accomplish both tasks simultaneously, outperforming single-task processing while also conserving computational resources. This suggests that multi-task processing of lumbar decomposition and landmark detection enhances the network's ability to learn spatial correspondences between the two tasks, thereby improving prediction accuracy for both tasks.

Table 3. Lumbar decomposition results. WO-FFM represents the multi-task network without the FFM module in our framework, while Single-task refers to the network using HRNet for single-task prediction.

| | | Dice | PSNR | SSIM |
|-----|-------------|--------------|-------------|--------------|
| AP | Ours | 0.995 | 45.8 | 0.992 |
| | WO-FFM | 0.994 | 45.5 | 0.991 |
| | Single-task | 0.994 | 45.7 | 0.992 |
| LAT | Ours | 0.993 | 43.0 | 0.988 |
| | WO-FFM | 0.992 | 42.4 | 0.987 |
| | Single-task | 0.992 | 42.7 | 0.988 |

Table 4. Accuracy of the landmark detection task (mm).

| | | endplate center | transverse process | pedicle | spinous process | Total |
|-----|-------------|-----------------|--------------------|-------------|-----------------|-------------|
| AP | Ours | 1.53 | 3.02 | 1.47 | 4.38 | 2.34 |
| | WO-FFM | 1.53 | 3.33 | 1.56 | 4.33 | 2.45 |
| | Single-task | 1.61 | 3.67 | 1.70 | 4.59 | 2.65 |
| LAT | Ours | 1.67 | 6.72 | 2.85 | 5.75 | 4.03 |
| | WO-FFM | 1.69 | 7.94 | 3.27 | 5.77 | 4.51 |
| | Single-task | 1.98 | 8.86 | 3.82 | 6.23 | 5.08 |

Table 5. SDR of the landmark detection task.

| | | endplate center | | | transverse process | | | pedicle | | | spinous process | | |
|-----|-------------|-----------------|-------------|-------------|--------------------|-------------|-------------|-------------|-------------|-------------|-----------------|-------------|-------------|
| | | 2mm | 4mm | 6mm | 2mm | 4mm | 6mm | 2mm | 4mm | 6mm | 2mm | 4mm | 6mm |
| | Ours | 74.5 | 98.5 | 99.9 | 30.3 | 75.7 | 94.5 | 76.9 | 98.6 | 99.9 | 19.1 | 50.1 | 75.1 |
| AP | WO-FFM | 74.5 | 98.5 | 99.9 | 26.1 | 68.0 | 91.7 | 73.7 | 98.0 | 99.8 | 20.3 | 51.2 | 76.0 |
| | Single-task | 72.9 | 98.1 | 99.7 | 21.9 | 63.3 | 87.5 | 70.7 | 97.7 | 99.5 | 18.7 | 47.9 | 72.1 |
| | Ours | 68.9 | 97.2 | 99.8 | 7.7 | 27.7 | 50.5 | 39.3 | 78.6 | 93.2 | 11.9 | 36.4 | 58.0 |
| LAT | WO-FFM | 67.9 | 97.7 | 99.8 | 7.1 | 22.2 | 40.2 | 29.3 | 71.9 | 91.1 | 9.6 | 33.9 | 58.8 |
| | Single-task | 66.9 | 97.2 | 99.1 | 4.9 | 17.6 | 34.6 | 25.2 | 64.9 | 87.1 | 8.1 | 29.9 | 54.8 |

The proposed method can accurately decompose five lumbar vertebrae in both AP and LAT lumbar X-ray images, achieving precise landmark detection (Fig. 7). The lumbar decomposition task was performed exceptionally well, with the network accurately identifying the five lumbar vertebrae and achieving precise decomposition. Landmark detection was more effective on AP images, while the localization of transverse processes in LAT images was less satisfactory. This discrepancy is mainly due to the overlap of transverse process vertices with adjacent structures, such as pedicles, which complicates precise localization in lateral views.

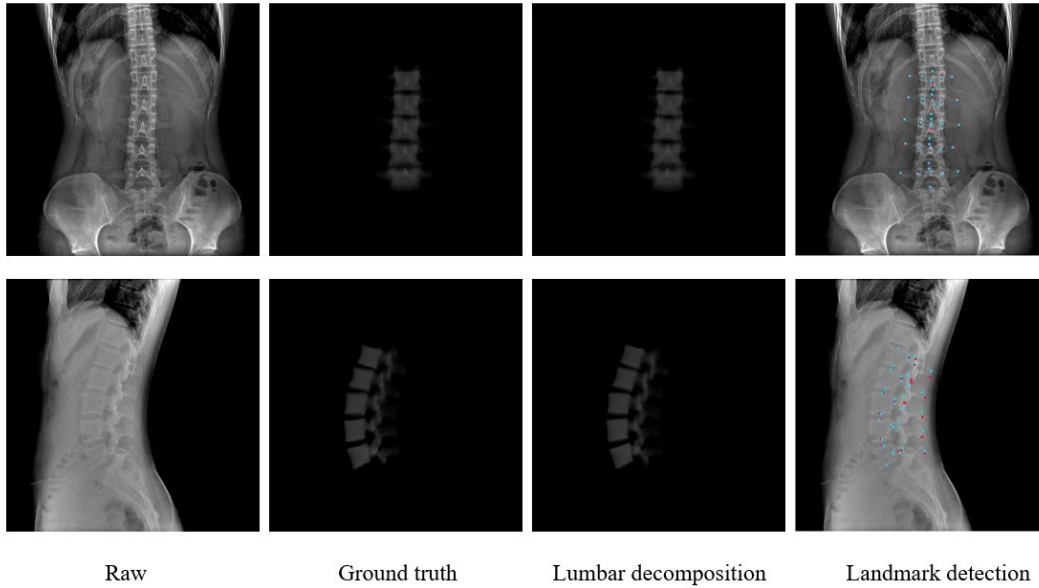


Fig. 7. Vertebra decomposition and landmark detection results output by the network. In the landmark detection result, blue marked points represent the ground truth, while red marked points indicate the predicted results.

We also used the trained model to make predictions on two cases of lumbar spine diseases: vertebral fusion and lumbar sacralization, with results depicted in Fig. 8. In the case of vertebral fusion, the model accurately decomposed the fused vertebrae, even though no similar samples were present in the training set. It successfully detected the endplate centers of the fused vertebrae and identified morphology resembling normal transverse processes. However, the detection results for the pedicles and spinous processes exhibited larger errors. In the lumbar sacralization case, we had

segmented the sacralized lumbar vertebra as L5 during the annotation process; however, the model only provided decomposition results for the first four lumbar vertebrae. Throughout the model training, all samples and annotated data were identified as five lumbar vertebrae. In this instance, the model failed to recognize L5 as integrated with the sacrum and did not classify T12 as a lumbar vertebra. This indicates that our model has the ability to determine whether a vertebral body is classified as a lumbar vertebra and does not mechanically predict five vertebrae.

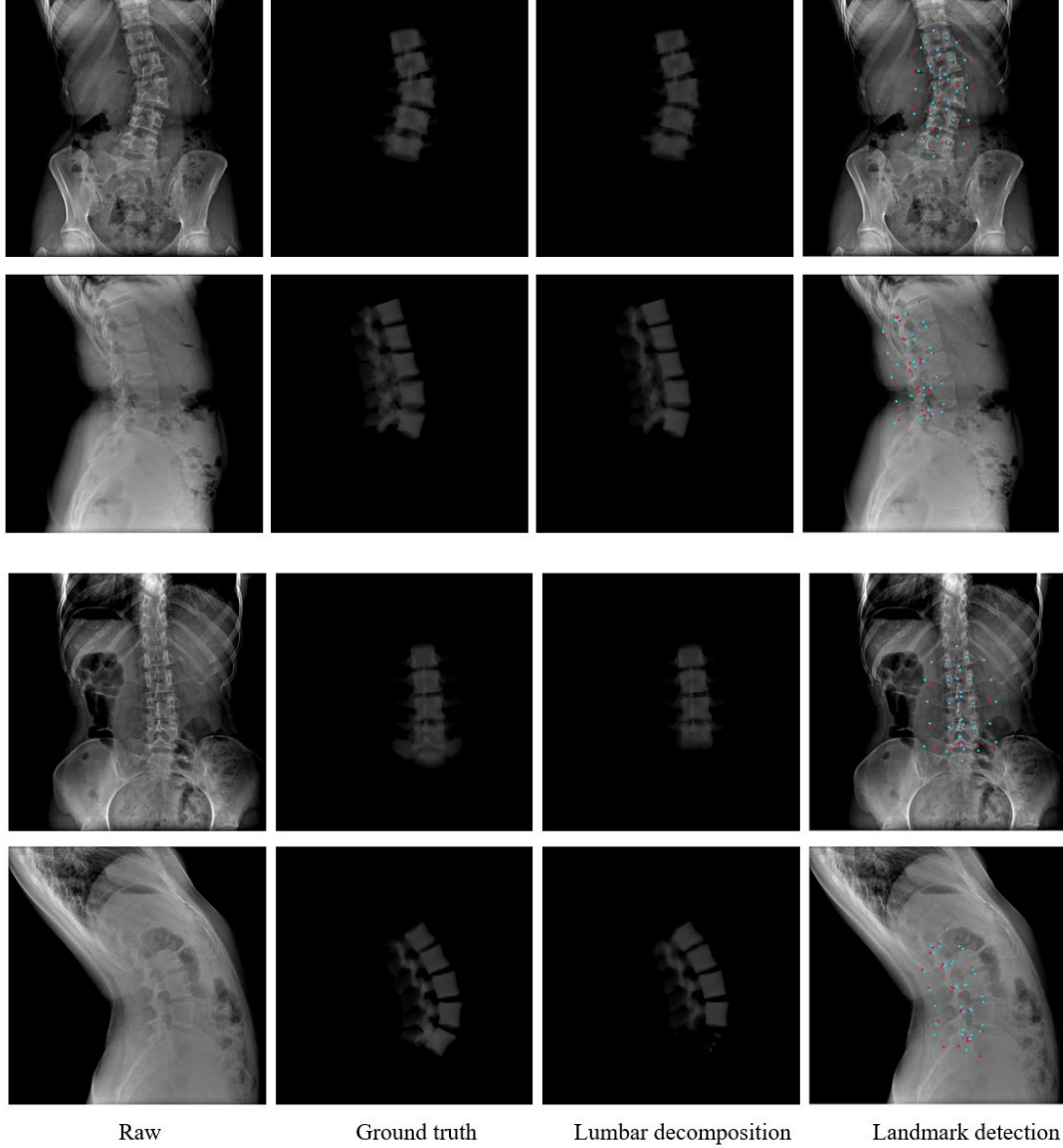


Fig. 8. Results of vertebral fusion and lumbar sacralization cases output by the network.

Ablation Experiments: We conducted ablation experiments on the FFM for the decomposition and landmark detection tasks in the proposed decoding process. The ablated network retained the shared HRNet encoder layers and included different output heads for each task. As shown in Tables 3-5, the model incorporating the FFM exhibited higher accuracy in both the lumbar decomposition and landmark detection tasks. Notably, in the LAT image task, the proposed method outperformed the network that lacked the FFM module by 0.5 mm in prediction accuracy.

3.3 3D reconstruction

Since the 3D reconstruction process was conducted in a predefined biplanar X-ray projection environment, we were able to directly compare the reconstruction results to the gold standard. We calculated the average vertice-to-face distance between the reconstructed model and the gold standard to measure the overall reconstruction error. Additionally, the Hausdorff distance was computed to quantify the maximum deviation. The test dataset included biplanar X-ray images from eight subjects in a 6-DOF bending state, resulting in a total of 144 pairs, which demonstrates the reconstruction capability of the proposed method for conditions such as scoliosis. Overall, the proposed method achieved a mean 3D reconstruction error of 0.80 ± 0.15 mm and a Hausdorff distance of 5.56 ± 1.29 mm (Table 6). Using the MAE as the loss function resulted in a mean reconstruction error of 0.93 ± 0.34 mm and a Hausdorff distance of 6.43 ± 2.00 mm. These results indicate that the proposed landmark-weighted reconstruction loss function yields lower reconstruction errors.

Table 6. Mean reconstruction error (mm) and Harsdorf distance (mm) for 3D Reconstruction. MAE represents the results obtained using simple average absolute error loss function.

| | | L1 | L2 | L3 | L4 | L5 | total |
|-----------|-------------|---------------------------------|---------------------------------|---------------------------------|---------------------------------|---------------------------------|---------------------------------|
| Mean | MAE | 0.90 \pm 0.32 | 0.91 \pm 0.30 | 0.91 \pm 0.36 | 0.92 \pm 0.38 | 1.01 \pm 0.34 | 0.93 \pm 0.34 |
| | Ours | 0.79\pm0.17 | 0.77\pm0.12 | 0.79\pm0.14 | 0.78\pm0.13 | 0.88\pm0.16 | 0.80\pm0.15 |
| Hausdorff | MAE | 6.15 \pm 1.68 | 6.18 \pm 1.94 | 6.08 \pm 2.04 | 6.74 \pm 2.27 | 6.99 \pm 1.90 | 6.43 \pm 2.00 |
| | Ours | 5.56\pm1.16 | 5.00\pm1.07 | 5.29\pm1.34 | 6.01\pm1.41 | 5.94\pm1.19 | 5.56\pm1.29 |

Additionally, we divided each vertebra into four regions: vertebral body, transverse process, articular process, and spinous process (Fig. 9), and evaluated the 3D reconstruction accuracy for each region using both loss functions. The reconstruction accuracy for the vertebral body was comparable between the two methods, while the transverse process, articular process, and spinous process were better reconstructed using the proposed landmark-weighted reconstruction loss function (Table 7, Fig. 10), with mean errors all below 1 mm.

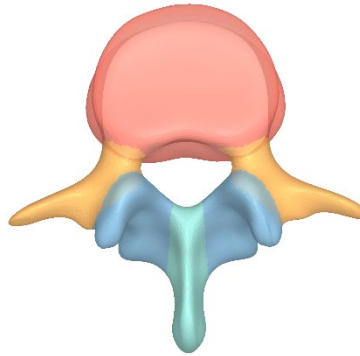


Fig. 9. The four regions of a vertebra: vertebral body (red), transverse processes (yellow), articular processes (blue), and spinous process (green).

Table 5. Mean reconstruction errors (mm) for different vertebral regions. MAE represents the results obtained using simple average absolute error loss function.

| | | L1 | L2 | L3 | L4 | L5 | total |
|--------------------|-------------|------------------|------------------|------------------|------------------|------------------|------------------|
| Vertebral body | MAE | 0.64±0.23 | 0.61±0.18 | 0.56±0.17 | 0.60±0.18 | 0.72±0.21 | 0.62±0.20 |
| | Ours | 0.65±0.22 | 0.58±0.12 | 0.55±0.11 | 0.58±0.11 | 0.72±0.19 | 0.62±0.17 |
| Transverse process | MAE | 0.97±0.43 | 1.19±0.46 | 1.29±0.66 | 1.16±0.51 | 1.17±0.51 | 1.16±0.53 |
| | Ours | 0.84±0.19 | 0.98±0.25 | 1.08±0.37 | 0.99±0.23 | 0.96±0.22 | 0.97±0.27 |
| Articular process | MAE | 1.01±0.36 | 0.99±0.33 | 1.00±0.39 | 1.06±0.42 | 1.17±0.39 | 1.04±0.39 |
| | Ours | 0.89±0.20 | 0.88±0.21 | 0.89±0.25 | 0.92±0.25 | 0.98±0.22 | 0.91±0.23 |
| Spinous process | MAE | 1.42±0.76 | 1.24±0.66 | 1.24±0.85 | 1.32±1.04 | 1.49±0.98 | 1.34±0.87 |
| | Ours | 0.96±0.34 | 0.81±0.20 | 0.87±0.22 | 0.85±0.23 | 1.08±0.35 | 0.91±0.29 |

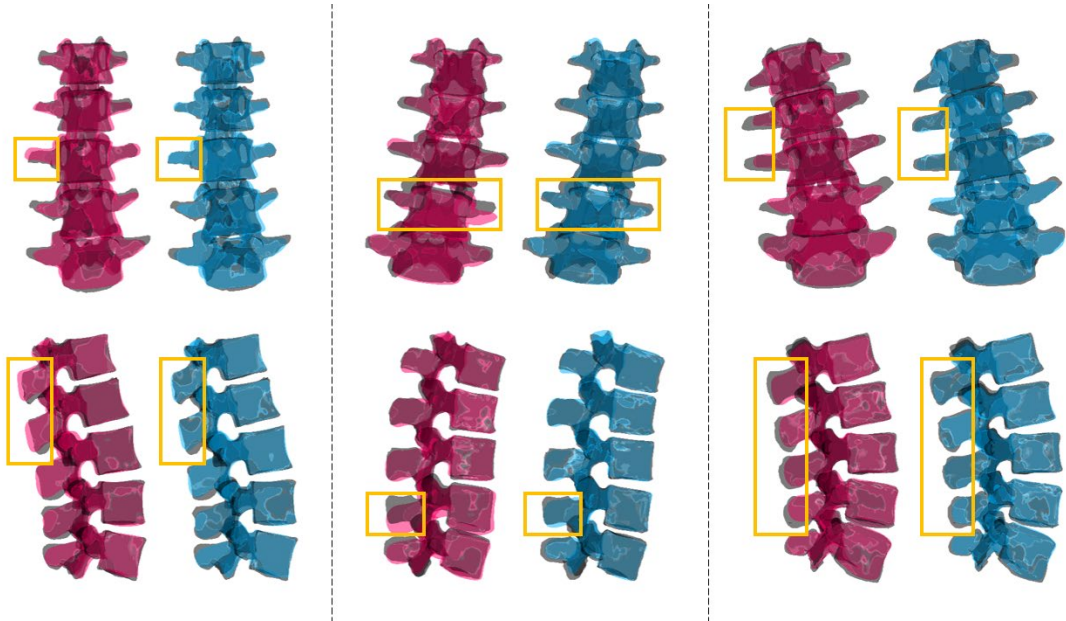


Fig. 10. 3D reconstruction results for three subjects. The black mesh represents the ground truth, the red mesh represents the reconstruction results using simple MAE loss function, and the blue mesh represents the reconstruction results using the landmark-weighted loss function.

We statistically analyzed the distribution of average errors between all reconstructed models and their corresponding ground truth (Fig. 10). Overall, reconstruction errors were lowest in the vertebral body, with larger errors mainly occurring in the transverse processes, spinous processes, and articular facets. These results demonstrate that the proposed landmark-weighted loss yields better reconstruction of fine structures in the posterior elements compared to the simple MAE loss.

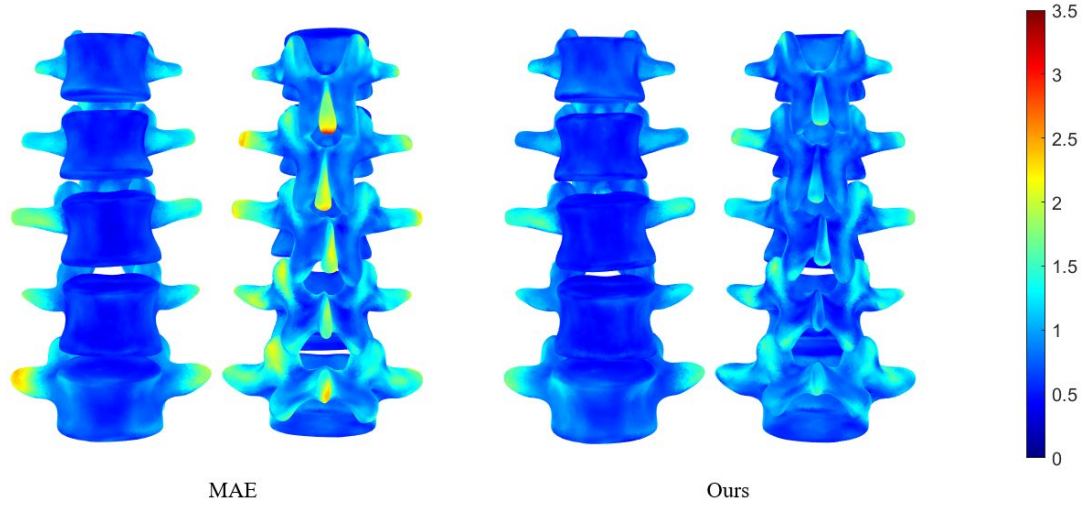


Fig. 11. Heatmap of average error distribution for 3D reconstruction. The color bar on the right represents the average error (mm) for different anatomical regions.

4 Discussion

This study demonstrates the feasibility of fully automated, high-precision reconstruction of lumbar vertebrae from biplanar X-ray images. We introduced a deep learning network for multi-task processing of lumbar decomposition and landmark detection for the first time, validating that the multi-task FFM enhances the accuracy of both tasks. Additionally, we proposed a landmark-weighted reconstruction loss function based on landmark positions, which effectively improves 3D reconstruction accuracy, particularly in the regions of the transverse and spinous processes. Finally, we utilized CT-segmented vertebrae from subjects and biplanar registration results as the gold standard to validate the accuracy of the 3D reconstruction. The results indicate that our proposed method achieves the highest accuracy in lumbar vertebrae 3D reconstruction to date.

Several previous works have achieved 3D reconstruction of the spine from biplanar X-ray images. Fang et al. proposed a method that combines X-ray images with CT models to reconstruct the 3D shape of the lumbar vertebrae, leveraging CT data to provide elastic shape meshes and intensity models for high-precision reconstruction (Fang et al., 2020). However, this method requires manual segmentation of the vertebrae from the X-ray images and is limited to 3D reconstructions of the L2, L3, and L4 vertebrae. Bennani et al. utilized uncalibrated X-ray images to reconstruct 3D lumbar vertebrae using a spherical demons algorithm to construct the vertebral shape model (Bennani et al., 2022). However, this method necessitates manually delineating the vertebrae's positions on the patient's dual-plane X-ray images with bounding boxes, preventing fully automated reconstruction. Aubert et al. introduced the use of a generative adversarial network (GAN) to convert the style of X-ray images to DRR, applying it to the registration of deformable spinal models with dual-plane images, achieving high-precision 3D spinal reconstruction (Aubert et al., 2023). However, the GAN used in this method generates processed output images that lack precise segmentation and do not fully retain the vertebrae in the raw X-ray images. Additionally, the fan-beam slot scanning system it uses is costly, making widespread clinical adoption difficult (Faria et al., 2013; Garg et al., 2020).

Currently, methods using deformable models for biplanar 3D reconstruction rely on mutual information or normalized cross-correlation as optimization functions during the registration

process (Reyneke et al., 2019). However, significant variations in vertebral shapes among individuals, compared to average shapes, along with the presence of soft tissues and other artifacts in biplanar X-ray images, lead to considerable errors in reconstructing fine structures such as the transverse and spinous processes (Aubert et al., 2019; Bennani et al., 2022). The method proposed in this study performs lumbar decomposition and landmark detection on the raw X-ray images using an encoder-decoder network architecture. Furthermore, it employs a landmark-weighted loss function during the 2D-3D registration process, achieving high-precision 3D reconstruction of the lumbar in a fully automated manner.

Regarding future research on improving the 3D reconstruction accuracy of biplanar X-ray images, we believe that optimization from the perspective of shape models could be beneficial. We have observed that, after achieving ultra-precise vertebra segmentation and DRR-style conversion, the main limitation in achieving a more accurate fit lies in the variability patterns of the SSM of the vertebrae. Due to limitations in data and computational resources, we could only select a finite number of principal components as optimization parameters. This constraint results in an inability to achieve high-precision reconstruction for individuals with rarer vertebral morphologies, and the method also falls short in reconstructing deformed vertebrae. Recent studies have explored direct end-to-end reconstruction from dual-plane images to 3D shapes using deep learning approaches (Ge et al., 2022), which theoretically could address issues related to deformed vertebrae. However, the accuracy of these methods needs improvement due to a lack of prior shape information about the vertebrae. Ultimately, using statistical shape models is one way to incorporate prior shape information of vertebrae into the 3D reconstruction process. Previous studies have accurately reconstructed personalized CT images from orthogonal X-ray images by regressing deformation fields containing shape statistical information from shape atlases or other auxiliary data (Van Houtte et al., 2022). Such deep learning networks that incorporate prior shape information of the object being reconstructed could be a significant direction for the development of ultra-sparse 3D reconstruction in the future.

Additionally, the resolution of the images used for reconstruction is a critical factor affecting accuracy. We utilized vertebra separation images predicted by a deep learning network, which had a resolution of 512×512 pixels and a pixel width of 0.834 mm. Considering the magnification effect of cone beam projections, the actual lumbar spine resolution would be higher. Thus, the proposed method achieves a 3D reconstruction accuracy close to the image resolution. While our study is limited by computational resources, future optimization efforts could explore using higher-resolution images to further enhance reconstruction accuracy.

This study has several limitations. Firstly, the lack of prior shape information for abnormal vertebrae during the establishment of the SSM makes it challenging to accurately reconstruct these vertebrae. Future research could consider establishing SSMs using a dataset that includes various types of deformed vertebrae. Secondly, the training and validation of this study were conducted using data from healthy subjects. Although the inclusion of 6-DOF bending positions of the lumbar vertebrae demonstrates the method's reconstruction capability in scenarios of spinal scoliosis, there is still a lack of real patient data to substantiate its clinical applicability. Lastly, the research utilized calibrated biplanar X-ray data for 3D reconstruction. Since biplanar X-ray imaging devices are not yet widely available in primary healthcare settings, future studies should explore how to perform 3D reconstruction using commonly available uncalibrated biplanar images.

5. Conclusion

We proposed and validated a method for fully automated 3D reconstruction of the lumbar spine from biplanar X-ray images. By performing lumbar decomposition and landmark detection on the raw X-ray images, and incorporating a landmark-weighted loss during the 3D reconstruction process, we enhanced the accuracy of laminae reconstruction and achieved better results for vertebrae with extreme morphologies. This method offers advantages such as low radiation exposure and full automation, serving as an auxiliary tool for X-ray diagnostics. It will support personalized diagnosis of conditions such as lumbar spondylolisthesis and intervertebral disc herniation in clinical settings. Furthermore, this method has the potential to be extended to the entire spine and other skeletal structures.

Data Availability Statement: Not applicable.

Ethics Approval Statement: The study was approved by the Institutional Review Board of Shanghai Tongji Hospital (protocol number: 2021-011-SK).

References:

- [1] Aubert, B., Cresson, T., de Guise, J.A., Vazquez, C., 2023. X-Ray to DRR Images Translation for Efficient Multiple Objects Similarity Measures in Deformable Model 3D/2D Registration. *IEEE Trans. Med. Imag.* 42, 897–909. <https://doi.org/10.1109/TMI.2022.3218568>
- [2] Aubert, B., Vazquez, C., Cresson, T., Parent, S., de Guise, J.A., 2019. Toward Automated 3D Spine Reconstruction from Biplanar Radiographs Using CNN for Statistical Spine Model Fitting. *IEEE Trans. Med. Imag.* 38, 2796–2806. <https://doi.org/10.1109/TMI.2019.2914400>
- [3] Audenaert, E.A., Van Houcke, J., Almeida, D.F., Paelinck, L., Peiffer, M., Steenackers, G., Vandermeulen, D., 2019. Cascaded statistical shape model based segmentation of the full lower limb in CT. *Comput. Methods Biomech. Biomed. Engin.* 22, 644–657. <https://doi.org/10.1080/10255842.2019.1577828>
- [4] Bennani, H., McCane, B., Cornwall, J., 2022. Three-dimensional reconstruction of In Vivo human lumbar spine from biplanar radiographs. *Comput. Med. Imaging Graph.* 96, 102011. <https://doi.org/10.1016/j.compmedimag.2021.102011>
- [5] Chen, Z., Guo, L., Zhang, R., Fang, Z., He, X., Wang, J., 2023. BX2S-Net: Learning to reconstruct 3D spinal structures from bi-planar X-ray images. *Comput. Biol. Med.* 154, 106615. <https://doi.org/10.1016/j.combiomed.2023.106615>
- [6] de Schepper, E.I.T., Overvest, G.M., Suri, P., Peul, W.C., Oei, E.H.G., Koes, B.W., Bierma-Zeinstra, S.M.A., Luijsterburg, P.A.J., 2013. Diagnosis of lumbar spinal stenosis: An updated systematic review of the accuracy of diagnostic tests. *Spine* 38, E469. <https://doi.org/10.1097/BRS.0b013e31828935ac>
- [7] Fang, L., Wang, Z., Chen, Z., Jian, F., Li, S., He, H., 2020. 3D shape reconstruction of lumbar vertebra from two X-ray images and a CT model. *IEEE/CAA J. Autom. Sinica* 7, 1124–1133. <https://doi.org/10.1109/JAS.2019.1911528>
- [8] Faria, R., McKenna, C., Wade, R., Yang, H., Woolacott, N., Sculpher, M., 2013. The EOS 2D/3D X-ray imaging system: A cost-effectiveness analysis quantifying the health benefits from reduced radiation exposure. *European Journal of Radiology* 82, e342–e349.

<https://doi.org/10.1016/j.ejrad.2013.02.015>

- [9] Galbusera, F., van Rijsbergen, M., Ito, K., Huyghe, J.M., Brayda-Bruno, M., Wilke, H.-J., 2014. Ageing and degenerative changes of the intervertebral disc and their impact on spinal flexibility. *Eur. Spine J.* 23, 324–332. <https://doi.org/10.1007/s00586-014-3203-4>
- [10] Garg, B., Mehta, N., Bansal, T., Malhotra, R., 2020. EOS® imaging: Concept and current applications in spinal disorders. *Journal of Clinical Orthopaedics and Trauma* 11, 786–793. <https://doi.org/10.1016/j.jcot.2020.06.012>
- [11] Ge, R., He, Y., Xia, C., Xu, C., Sun, W., Yang, G., Li, J., Wang, Z., Yu, H., Zhang, D., Chen, Y., Luo, L., Li, S., Zhu, Y., 2022. X-CTRSNet: 3D cervical vertebra CT reconstruction and segmentation directly from 2D X-ray images. *Knowledge-Based Systems* 236, 107680. <https://doi.org/10.1016/j.knosys.2021.107680>
- [12] Gheno, R., Nectoux, E., Herbaux, B., Baldisserotto, M., Glock, L., Cotten, A., Boutry, N., 2012. Three-dimensional measurements of the lower extremity in children and adolescents using a low-dose biplanar X-ray device. *Eur. Radiol.* 22, 765–771. <https://doi.org/10.1007/s00330-011-2308-y>
- [13] Gupta, A., Kharbanda, O.P., Sardana, V., Balachandran, R., Sardana, H.K., 2016. Accuracy of 3D cephalometric measurements based on an automatic knowledge-based landmark detection algorithm. *Int. J. Comput. Ass. Rad.* 11, 1297–1309. <https://doi.org/10.1007/s11548-015-1334-7>
- [14] Gupta, A., Kharbanda, O.P., Sardana, V., Balachandran, R., Sardana, H.K., 2015. A knowledge-based algorithm for automatic detection of cephalometric landmarks on CBCT images. *Int. J. Comput. Ass. Rad.* 10, 1737–1752. <https://doi.org/10.1007/s11548-015-1173-6>
- [15] Hasegawa, K., Okamoto, M., Hatsushikano, S., Caseiro, G., Watanabe, K., 2018. Difference in whole spinal alignment between supine and standing positions in patients with adult spinal deformity using a new comparison method with slot-scanning three-dimensional X-ray imager and computed tomography through digital reconstructed radiography. *BMC Musculoskeletal Disorders* 19, 437. <https://doi.org/10.1186/s12891-018-2355-5>
- [16] Karade, V., Ravi, B., 2015. 3D femur model reconstruction from biplane X-ray images: a novel method based on Laplacian surface deformation. *Int. J. Comput. Ass. Rad.* 10, 473–485. <https://doi.org/10.1007/s11548-014-1097-6>
- [17] Klima, O., Kleparnik, P., Spanel, M., Zemcik, P., 2016. Intensity-based femoral atlas 2D/3D registration using Levenberg-Marquardt optimisation, in: *Medical Imaging 2016: Biomedical Applications in Molecular, Structural, and Functional Imaging*. Presented at the Medical Imaging 2016: Biomedical Applications in Molecular, Structural, and Functional Imaging, SPIE, pp. 113–124. <https://doi.org/10.1117/12.2216529>
- [18] Li, Guoan, Wang, S., Passias, P., Xia, Q., Li, Gang, Wood, K., 2009. Segmental in vivo vertebral motion during functional human lumbar spine activities. *Eur Spine J* 18, 1013–1021. <https://doi.org/10.1007/s00586-009-0936-6>
- [19] Liang, Z., Wang, Q., Xia, C., Chen, Z., Xu, M., Liang, G., Yu Zhang, Ye, C., Zhang, Y., Yu, X., Wang, H., Zheng, H., Du, J., Li, Z., Tang, J., 2024. From 2D to 3D: automatic measurement of the Cobb angle in adolescent idiopathic scoliosis with the weight-bearing 3D imaging. *Spine J.* 24, 1282–1292. <https://doi.org/10.1016/j.spinee.2024.03.019>
- [20] Markelj, P., Tomaževič, D., Likar, B., Pernuš, F., 2012. A review of 3D/2D registration methods for image-guided interventions. *Med. Image Anal., Computer Assisted Interventions* 16, 642–

661. <https://doi.org/10.1016/j.media.2010.03.005>

- [21] Matz, P.G., 2016. Guideline summary review: an evidence-based clinical guideline for the diagnosis and treatment of degenerative lumbar spondylolisthesis. *Spine J.* <https://doi.org/10.1016/j.spinee.2015.11.055>
- [22] Miao, S., Wang, Z.J., Liao, R., 2016. A CNN Regression Approach for Real-Time 2D/3D Registration. *IEEE Trans. Med. Imag.* 35, 1352–1363. <https://doi.org/10.1109/TMI.2016.2521800>
- [23] Pointon, J.L., Wen, T., Tugwell-Allsup, J., Sújar, A., Létang, J.M., Vidal, F.P., 2023. Simulation of X-ray projections on GPU: Benchmarking gVirtualXray with clinically realistic phantoms. *Comput. Methods Programs Biomed.* 234, 107500. <https://doi.org/10.1016/j.cmpb.2023.107500>
- [24] Reyneke, C.J.F., Lüthi, M., Burdin, V., Douglas, T.S., Vetter, T., Mutsvangwa, T.E.M., 2019. Review of 2-D/3-D Reconstruction Using Statistical Shape and Intensity Models and X-Ray Image Synthesis: Toward a Unified Framework. *IEEE Rev. Biomed. Eng.* 12, 269–286. <https://doi.org/10.1109/RBME.2018.2876450>
- [25] Sarkalkan, N., Weinans, H., Zadpoor, A.A., 2014. Statistical shape and appearance models of bones. *Bone* 60, 129–140. <https://doi.org/10.1016/j.bone.2013.12.006>
- [26] Sun, K., Zhao, Y., Jiang, B., Cheng, T., Xiao, B., Liu, D., Mu, Y., Wang, X., Liu, W., Wang, J., 2019. High-Resolution Representations for Labeling Pixels and Regions. <https://doi.org/10.48550/arXiv.1904.04514>
- [27] Tan, S., Yao, J., Yao, L., Ward, M.M., 2013. High precision semiautomated computed tomography measurement of lumbar disk and vertebral heights. *Medical Physics* 40, 011905. <https://doi.org/10.1118/1.4769412>
- [28] Väänänen, S.P., Grassi, L., Flivik, G., Jurvelin, J.S., Isaksson, H., 2015. Generation of 3D shape, density, cortical thickness and finite element mesh of proximal femur from a DXA image. *Med. Image Anal.* 24, 125–134. <https://doi.org/10.1016/j.media.2015.06.001>
- [29] Van Houtte, J., Audenaert, E., Zheng, G., Sijbers, J., 2022. Deep learning-based 2D/3D registration of an atlas to biplanar X-ray images. *Int J CARS* 17, 1333–1342. <https://doi.org/10.1007/s11548-022-02586-3>
- [30] Wang, X.-R., Xu, F.-R., Huang, Q.-L., Wáng, Y.X.J., 2020. Radiological features of traumatic vertebral endplate fracture: an analysis of 194 cases with 263 vertebral fractures. *Chin. Med. J. (engl.)* 133, 2696–2702. <https://doi.org/10.1097/CM9.0000000000000919>
- [31] Wáng, Y.X.J., Deng, M., He, L.-C., Che-Nordin, N., Santiago, F.R., 2018. Osteoporotic vertebral endplate and cortex fractures: A pictorial review. *Journal of Orthopaedic Translation, Orthopaedic imaging for translational research and clinical application* 15, 35–49. <https://doi.org/10.1016/j.jot.2018.08.004>
- [32] Whitmarsh, T., Humbert, L., Del Río Barquero, L.M., Di Gregorio, S., Frangi, A.F., 2013. 3D reconstruction of the lumbar vertebrae from anteroposterior and lateral dual-energy X-ray absorptiometry. *Med. Image Anal.* 17, 475–487. <https://doi.org/10.1016/j.media.2013.02.002>
- [33] Wybier, M., Bossard, P., 2013. Musculoskeletal imaging in progress: The EOS imaging system. *Joint Bone Spine* 80, 238–243. <https://doi.org/10.1016/j.jbspin.2012.09.018>
- [34] Yi, J., Wu, P., Huang, Q., Qu, H., Metaxas, D.N., 2020. Vertebra-Focused Landmark Detection for Scoliosis Assessment, in: 2020 IEEE 17th International Symposium on Biomedical Imaging (ISBI). Presented at the 2020 IEEE 17th International Symposium on Biomedical

Imaging (ISBI), pp. 736–740. <https://doi.org/10.1109/ISBI45749.2020.9098675>

- [35] Yu, W., Chu, C., Tannast, M., Zheng, G., 2016. Fully automatic reconstruction of personalized 3D volumes of the proximal femur from 2D X-ray images. *Int. J. Comput. Ass. Rad.* 11, 1673–1685. <https://doi.org/10.1007/s11548-016-1400-9>